JOURNAL OF SOLID STATE CHEMISTRY **130,** 117–128 (1997)
ARTICLE NO. SC977287

$LaMnO_{3+\delta}$ Revisited

J. Töpfer[1] and J. B. Goodenough

Center for Materials Science and Engineering, ETC II 9.104, The University of Texas at Austin, Austin, Texas, 78712

Received September 26, 1996; in revised form January 15, 1997; accepted January 22, 1997

Samples of $LaMnO_{3+\delta}$ with $0 \leq \delta \leq 0.18$ have been prepared via a precipitation method followed by heating at different temperatures and oxygen partial pressures. Oxidation is accommodated by the formation of cation vacancies to give $La_{1-\varepsilon}Mn_{1-\varepsilon}O_3$ with $\varepsilon = \delta/(3+\delta)$. Room temperature X-ray diffraction reveals a two-phase region separating an O′-orthorhombic phase stable over $0 \leq \delta \leq 0.06$ and a rhombohedral phase, stable in the range $0.10 \leq \delta \leq 0.18$, that transforms below room temperature to an O′-orthorhombic phase. Transport and magnetic studies indicate the following evolution of electronic properties with increasing δ. Oxidation creates small-polaron holes that become increasingly trapped at cation vacancies with decreasing temperature in the paramagnetic domain. Some of these trapped holes are released on cooling through the onset of long-range magnetic order. In the O′-orthorhombic structure, the trapped holes form superparamagnetic clusters below room temperature that become magnetically coupled with the onset of antiferromagnetic order in the hole-poor matrix to form a magnetic glass. The O′-orthorhombic structure sustains the cooperative Jahn–Teller deformation. The rhombohedral phase suppresses the cooperative Jahn–Teller deformation, and the hole-poor matrix becomes ferromagnetic. With increasing δ, the perovskite tolerance factor increases, and at a critical value $t_c \approx 0.97$, a transition from small-polaron to a peculiar nondispersive delocalized state of the conduction electrons occurs below T_c. At highest δ, these conduction electrons introduce a double-exchange spin–spin coupling in the matrix that varies as $\cos(\theta_{ij}/2)$; this ferromagnetic coupling competes with the antiferromagnetic Mn: t^3–O: $2p_\pi$–Mn: t^3 superexchange, which varies as $\cos\theta_{ij}$. Consequently an equilibrium θ_{ij} increases with δ to give a cant angle $0^\circ \leq \theta \leq 180^\circ$, which introduces metamagnetic behavior of the matrix between clusters and a ferromagnetic magnetization that decreases relatively sharply with increasing δ in the range $0.13 \leq \delta \leq 0.18$.

INTRODUCTION

Early attempts to prepare the perovskite $LaMnO_3$ showed that it is oxidized with firing in air; stoichiometry was approached by firing at lower oxygen activities (1). Although characterized at the time as $LaMnO_{3+\delta}$, it was realized that the perovskite structure cannot accept excess oxygen in an interstitial site. However, the nonstoichiometry δ is accommodated as cation vacancies, as has been shown by several studies on the defect chemistry of that material either by TGA measurements (2–4) or diffraction experiments (3, 5, 6). Accordingly, the composition of $LaMnO_{3+\delta}$ is better expressed as $La_{1-\varepsilon}Mn_{1-\varepsilon}O_3$ with $\varepsilon = \delta/(3+\delta)$ or

$$LaMn^{3+}_{1-2\delta}Mn^{4+}_{2\delta}O_{3+\delta} = \frac{3+\delta}{3}La_{3/3+\delta}\square_{\delta/3+\delta}Mn^{3+}_{(3-6\delta)/3+\delta}Mn^{4+}_{6\delta/3+\delta}\square_{\delta/3+\delta}O_{3.00}. \quad [1]$$

Since we determine analytically the ratio $La/O = Mn/O = 3+\delta$, we refer in this paper to the system $LaMnO_{3+\delta}$; the conversion to $La_{1-\varepsilon}Mn_{1-\varepsilon}O_3$ is straightforward.

Most studies of the manganese oxides with the perovskite structure have concentrated on the properties of the $La_{1-x}A_xMnO_3$ systems containing a larger rare-earth atom such as Ln = La, Pr, or Nd and a larger alkaline-earth atom A = Ca, Sr, or Ba. Recent interest in this family of materials has been stimulated by the observation of a "colossal" negative magnetoresistance (CMR) in alkaline-earth doped manganites (7) and by the charge-ordering transition near $x = 0.5$ (8) that was first recognized (9) in the $La_{1-x}Ca_xMnO_3$ system in an interpretation of the magnetic order found by neutron diffraction (10). The occurrence of CMR has also been reported for $LaMnO_{3+\delta}$ (11).

In the parent compound $LnMnO_3$, the mismatch between equilibrium Ln–O and Mn–O bond lengths is given by a tolerance factor

$$t = \frac{(Ln\text{–O})}{\sqrt{2}(\text{Mn–O})} \quad [2]$$

that decreases with decreasing temperature. The cubic perovskite adjusts to a $t < 1$ by a cooperative rotation of the

[1] To whom correspondence should be addressed at the present address: Hermsdorfer Institut für Technische Keramik, Naumburger Strasse, 07629 Hermsdorf, Germany.

0022-4596/97 $25.00

MnO_6 octahedra that buckles the Mn–O–Mn bond angle from 180° to (180° − ϕ), where ϕ increases with decreasing t to lower the space group symmetry from cubic to tetragonal, rhombohedral, or orthorhombic. In the parent perovskite $LaMnO_3$, the symmetry is lowered to orthorhombic by a cooperative rotation of the MnO_6 octahedra around the cubic [1 1 0] axis as in $GdFeO_3$ (12). Superimposed on this distortion is a cooperative Jahn–Teller deformation setting in well above room temperature that removes the orbital degeneracy of the localized, high spin ^5E_g electronic configuration at the octahedral-site $Mn^{3+}: t_2^3 e^1$ ions; a cooperative shifting of each O^{2-} ion of an a–b plane away from one of its two near-neighbor Mn atoms toward the other creates long and short O–Mn–O bond lengths perpendicular to each other at each Mn atom, the long bonds rotating 90° within an a–b plane on going from one Mn atom to another (9). The Jahn–Teller deformation lowers the $c/\sqrt{2}a$ ratio to less than unity without any further lowering of the space group symmetry from orthorhombic (*Pbnm*).

The Jahn–Teller electronic ordering couples the Mn^{3+} spins $S = 2$ ferromagnetically within the a–b planes of the parent $LaMnO_3$ compound via a dominant e^1–O: $2p_\sigma$–e^0 superexchange interaction; these planes are coupled antiparallel to one another via t_2^3–O: $2p_\pi$–t_2^3 superexchange interactions, which are dominant along the c axis. This A-type antiferromagnetic order is modified by the cooperative rotation of the MnO_6 octahedra about the orthorhombic b axis, which introduces an antisymmetric Dzialoshinski exchange coupling $D_{ij} \cdot S_i \times S_j$ that cants the antiparallel coupling to give a weak canted-spin ferromagnetism.

The end member $CaMnO_3$ is an antiferromagnetic insulator; each localized electronic configuration $^4A_{2g}$ at a $Mn^{4+}: t_2^3\, e^0$ ion has its spin $S = 3/2$ coupled antiparallel to its six neighbors (Type-G antiferromagnetic order) via t_2^3–O: $2p_\pi$–t_2^3 superexchange interactions. The t_2^3 configurations of a Mn^{4+}/Mn^{3+} couple remain localized over the entire compositional range $0 \le x \le 1$ of a $La_{1-x}A_xMnO_3$ system. The σ-antibonding e electrons, on the other hand, undergo a transition from localized to itinerant character with increasing x; the CMR effect is a maximum at the crossover from localized $-e$ to itinerant $-\sigma^*$ electronic behavior below T_c (7). Moreover, the itinerant σ^* electrons introduce a global ferromagnetic coupling, and by $x = 0.3$ the systems $La_{1-x}A_xMnO_3$ are ferromagnetic metals below the Curie temperature T_c.

In this paper we explore the transition from polaronic to itinerant behavior of the Mn e electrons in the system $LaMnO_{3+\delta}$ where the introduction of cation vacancies in the MnO_3 array strongly perturbs any antibonding itinerant-electron σ^* band states of e-orbital parentage. Earlier studies showed that $LaMnO_{3+\delta}$ undergoes a transition from polaronic behavior and antiferromagnetic order at low values of δ to a ferromagnetic metal at $\delta \approx 0.12$ (13, 14).

EXPERIMENTAL

$LaMnO_{3+\delta}$ samples were prepared by a wet chemical precipitation route. La_2O_3 (dried before use at 950°C) and $MnCO_3$ (Mn-content gravimetrically determined) were subsequently dissolved in acetic acid. To obtain a clear solution, a few crystals of hydroxyl aminochloride were added to reduce higher valent manganese ions. A solution of citric acid was added to the hot solution of the metal ions, and a white precipitate was obtained. The solution was slowly evaporated on a hot plate, and the obtained solid was calcined at 800°C. The precursor powders were pressed into pellets and fired at 1300°C for 24 h in air. Then the pellets were crushed in an agate mortar, pressed again into pellets, and sintered again at 1300°C for 24 h in air. After that, final equilibration runs under a given set of conditions (Table 1) were performed in either argon, air, or oxygen. The oxygen partial pressure in the argon used was independently determined with the help of an EMF cell based on doped zirconia; the measured cell voltage indicated an oxygen partial pressure of about 10^{-5} atm. Samples heated in argon or oxygen were slowly cooled down in the furnace in the gas atmosphere, and those heated in air were quenched. To obtain higher concentrations of Mn^{4+}, samples were prepared by direct heating of pellets of the precursor powder at 800°C in oxygen. Another set of samples was synthesized by sintering pellets of the starting precursor material at 1000°C for 24 h in air before a final equilibration run at 800°C in oxygen was carried out.

The products were checked by powder X-ray diffraction with Cu$K\alpha$ radiation and Si as internal standard. The nonstoichiometry parameter δ was determined by chemical titration: the samples were dissolved in an excess of VO^{2+} in sulfuric acid and potentiometrically titrated with $KMnO_4$ solution. This procedure was checked with Mn_3O_4, and an accuracy of $O_{3.00 \pm 0.01}$, referred to as AMO_3, was achieved.

Magnetic properties of the products were measured with a Quantum Design MPMS SQUID magnetometer. Susceptibility measurements were performed in a zero-field-cooled (ZFC) and in a field-cooled (FC) mode in a field of 100 Oe. The field dependence of the magnetization and hysteresis loops $M = M(H)$ were recorded at 5 K on field-cooled samples.

The electrical resistance of the sintered pellets was measured between 30 and 300 K in a four-probe device. Seebeck coefficients were obtained from measurements in home-built devices between 30–300 K and 300–1000 K; the high-temperature measurements were performed in air. Thermal analysis of the materials was carried out with a Perkin–Elmer thermal analysis system. TGA runs were performed

in various gas atmospheres with a heating/cooling rate of 1 K/min.

RESULTS

1. Sample Preparation and X-Ray Characterization

The nonstoichiometry of the samples of $LaMnO_{3+\delta}$ as determined by redox titration is summarized in Table 1 together with the firing conditions. Heating at 1200°C at log $P_{O_2} \approx -5$ gives the stoichiometric perovskite with $\delta = 0.00$, while heating in air at 1200°C results in $\delta = 0.05$. Lowering the temperature in air or oxygen leads to samples with higher concentrations of cation vacancies and Mn^{4+}. The values of δ obtained are in good agreement with results of thermogravimetric studies on the deviation from stoichiometry as a function of temperature and oxygen partial pressure (2, 4). Dense samples, which were first sintered at 1300°C and then heated at lower temperatures, could not be oxidized higher than $\delta = 0.13$; even prolonged firing at 700°C in oxygen did not increase the Mn^{4+} concentration. Therefore samples were either heated at only 1000°C before a final anneal at 800°C in oxygen or annealed at 800°C without any prefiring of the precursor material. As a result of this procedure, higher δ values were accessible; however, the densities of these samples were considerably lower than those of samples prefired at 1300°C.

The room temperature X-ray patterns of some of the samples are shown in Fig. 1. $LaMnO_{3+\delta}$ with $0 \leq \delta \leq 0.06$ crystallizes in the orthorhombic $GdFeO_3$ structure (*Pbnm*) at room temperature; all reflections could be indexed on the basis of the orthorhombic cell. This is in agreement with a recent neutron-diffraction study on a sample with $\delta = 0.005$ (15). A monoclinic structure, as proposed for small δ in the system $La_{1-x}Sr_xMnO_3$ (16), has not been observed. The orthorhombicity decreases with increasing δ, i.e., with increasing tolerance factor t. It is noteworthy that at room temperature all the orthorhombic samples fulfill the criterion $c/a < \sqrt{2}$ characteristic of a cooperative Jahn–Teller deformation superimposed on the orthorhombic structure resulting from $t < 1$. For $\delta > 0.09$, the rhombohedral structure ($R\bar{3}c$) is observed with the rhombohedral angle α decreasing with increasing δ or t. This is in good agreement with other studies (1, 14). Two representative X-ray patterns of samples with rhombohedral room temperature structure are displayed in Fig. 1. The reflections of the sample with $\delta = 0.18$ are broadened due to a small particle size; this sample was prepared at 800°C in oxygen without an intermediate high-temperature firing. The evolution of the lattice parameters is shown in Fig. 2. Between the orthorhombic and rhombohedral phase field, a two-phase region was observed; the sample with $\delta = 0.07$ exhibits reflections of both phases. Deviations from the regular evolution (Vegard's law) of the cell parameters were found on both sides of this composition, indicating an onset of the two-phase field. The exact width of this region is not known. However, a similar two-phase field between orthorhombic and rhombohedral compounds of the system $La_{1-x}Sr_xMnO_3$ has been reported (16).

2. Magnetic Properties

The temperature dependence of the inverse magnetic susceptibility of samples measured in a field of 100 Oe with

TABLE 1
Preparation Conditions, Values of δ as Determined by Titration, Lattice Parameters, Effective Magnetic Moment Extracted from the Curie–Weiss Part of the $1/\chi$ vs T Curves (300–600 K) and Calculated Magnetic Moment (Spin-Only) for $LaMnO_{3+\delta}$ Compounds

T and gas atmosphere	δ	a (Å)	b (Å)	c (Å)	α (°)	μ_{eff}	μ_{so}
A. Initial firing 1300°C							
24 h, 1200°C Ar	0.00	5.532(4)	5.738(1)	7.693(5)		5.55	4.90
24 h, 1300°C air	0.04	5.542(2)	5.658(2)	7.711(2)			
24 h, 1200°C air	0.05	5.537(2)	5.656(2)	7.715(3)		6.19	4.81
24 h, 1100°C air	0.06	5.543(4)	5.598(4)	7.765(6)			
24 h, 1000°C air	0.07					5.92	4.72
24 h, 900°C air	0.09	5.503(2)			60.40(1)		
24 h, 850°C air	0.10	5.480(1)			60.72(1)		
48 h, 800°C O_2	0.11	5.472(1)			60.68(1)	5.49	4.61
48 h, 750°C O_2	0.12	5.476(1)			60.69(1)		
100 h, 700°C O_2	0.13	5.471(1)			60.63(1)		
B. Initial firing 1000°C							
48 h, 800°C O_2	0.14	5.469(1)			60.58(1)		
C. No initial firing							
50 h, 800°C O_2	0.16						
100 h, 800°C O_2	0.18	5.471(2)			60.54(1)	4.86	4.43

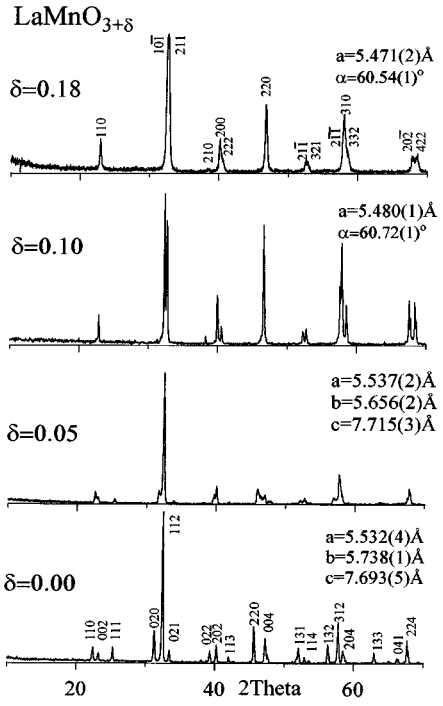

FIG. 1. Examples of room temperature X-ray diffraction powder patterns (Cu$K\alpha$) for orthorhombic perovskites ($\delta = 0.00$, 0.05) and rhombohedral perovskites ($\delta = 0.10$, 0.18).

heating after cooling in zero field (ZFC) is shown in Fig. 3. All samples exhibit a ferromagnetic Weiss constant θ_p that increases with δ. The onset of magnetic long-range order below a critical temperature ranges from $T_N = 135$ K for $\delta = 0.00$ to $T_c = 240$ K for $\delta = 0.18$. Each sample shows a ferromagnetic component below the ordering temperature. The Curie temperatures of the samples with $0.05 \leq \delta \leq 0.11$ are at about 170–180 K. In Table 1, the effective magnetic moments μ_{eff} extracted from the paramagnetic range are compared to the magnetic moments based on

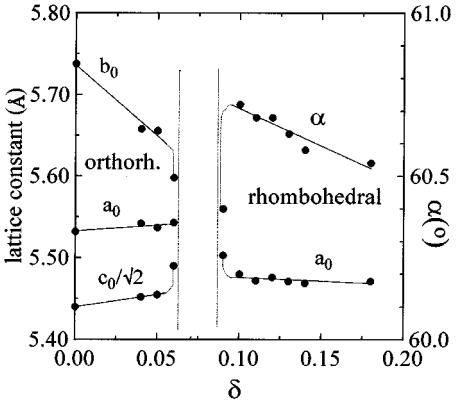

FIG. 2. Variation of room temperature cell parameters with δ for $LaMnO_{3+\delta}$.

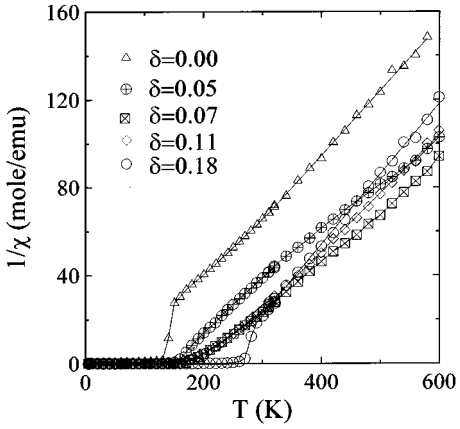

FIG. 3. Temperature dependence of the inverse magnetic susceptibility of $LaMnO_{3+\delta}$ samples measured in a field of 100 Oe.

spin-only contributions; the experimental values are considerably larger than expected. In addition, the curves $1/\chi(T)$ are not linear above T_c, and a change of the slope occurs near 300 K.

In Fig. 4 the molar magnetizations measured between 5 and 300 K in a field of 100 Oe for samples with $\delta = 0.05$ and $\delta = 0.18$ are compared; both zero-field-cooled (ZFC) and field-cooled (FC) runs are shown. Whereas the ZFC measurements exhibit a broad maximum in $M(T)$ below T_c, no such maximum is found for the FC runs in which $M(T)$ decreases with temperature and is almost temperature-independent at low temperatures. The difference between the FC and ZFC magnetization at low temperature becomes smaller in the rhombohedral phase.

Figure 5 shows the field dependence at 5 K of several samples in a field up to 40 kOe. The following observations are noted: (i) at higher δ the samples become saturated at the maximum applied field, and at lower δ they do not become

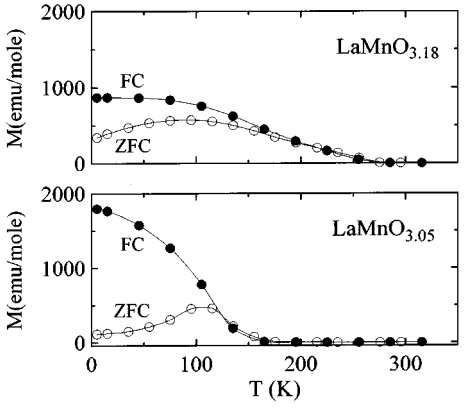

FIG. 4. Zero-field-cooled (ZFC) and field-cooled (FC) magnetization for $\delta = 0.05$ and $\delta = 0.18$.

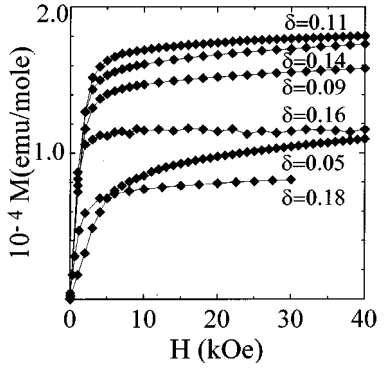

FIG. 5. Field dependence of the molar magnetization at 5 K for samples with various values of δ (sample with $\delta = 0.18$ only measured to 30 kOe).

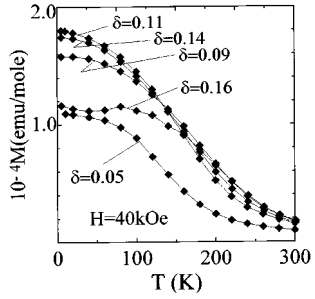

FIG. 7. Temperature variation of the magnetization in a field of 40 kOe for samples with various values of δ.

totally saturated; and (ii) the saturation magnetization (taken as magnetization at maximum field) increases with δ to a maximum value at around $\delta = 0.12$. The evolution with δ of the number of Bohr magnetons, calculated from the magnetization data at maximum field, is plotted in Fig. 6. At $\delta \approx 0.12$, the magnetization approaches the theoretical value expected for full aligment of the spins (straight line at the top of the graph), but for $\delta > 0.12$ it decreases with increasing δ. The inset of Fig. 6 shows the $M = M(H)$ curves of the samples with $\delta = 0.05$ and 0.18 at 5 K. The sample with $\delta = 0.18$ shows saturated moments at a field of 30 kOe, the sample with $\delta = 0.05$ is not yet saturated under that field. The area of the hysteresis loops and the remanence are small. In Fig. 7 the temperature variation of the magnetization in a field of 40 kOe is plotted. Compared to the low-field magnetization data of Fig. 4, the absolute values of M are much larger and the decrease in M with increasing temperature is smoother. Whereas samples with smaller values of δ show a regular shape of the $M(T)$ curve, the $\delta = 0.16$ sample is anomalous below 90 K.

3. *Transport Properties*

Measurements of the thermoelectric power as a function of temperature, $\alpha(T)$, between 30 and 1000 K are shown in Fig. 8 for selected samples. From these plots we note several features: (i) all samples show a maximum in the $\alpha(T)$ curves between 140–220 K and the absolute values of α at this maximum temperature, $T_{\alpha(\max)}$, increase with decreasing δ; (ii) the thermopower of samples with smaller δ could not be measured at very low temperatures because of a high sample impedance whereas $\alpha(T)$ drops to values close to 0 μV/K below 100 K in samples with $\delta \geq 0.13$; and (iii) at temperatures $T > T_{\alpha(\max)}$ the Seebeck coefficient decreases to small positive or negative values at high temperatures, becoming

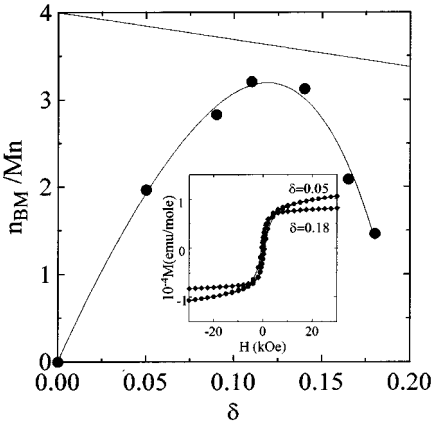

FIG. 6. Variation with δ of the magnetic moments per Mn ion at 5 K obtained from saturation magnetizations taken at 40 kOe (30 kOe for $\delta = 0.18$). (Inset) Plot of the magnetization vs field at 5 K for $\delta = 0.05$ and $\delta = 0.18$.

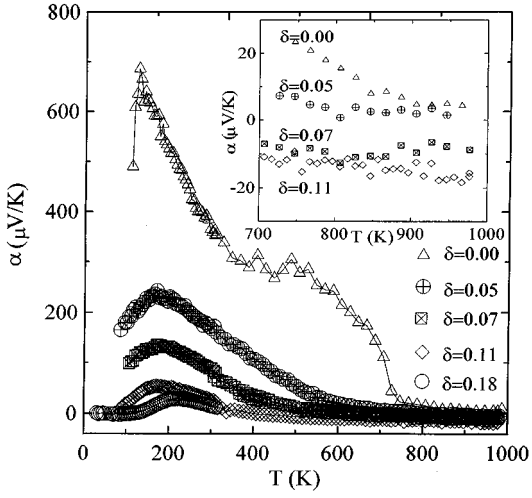

FIG. 8. Thermopower α for selected samples of $LaMnO_{3+\delta}$ as a function of temperature. (Inset) Thermopower α as a function of T in the temperature range 700–1000 K.

temperature-independent above 800 K. The evolution of $\alpha(T)$ in the temperature range 700–1000 K is shown in the inset of Fig. 8; it is consistent with a small-polaron model described by

$$\alpha = -\frac{k}{e}\ln\left(\beta\frac{1-c}{c}\right), \qquad [3]$$

where $c = n/N$ is the fractional occupancy of N Mn sites by mobile charge carriers and β is a spin-degeneracy factor. From the values of α at high temperatures (e.g., $\alpha = 5\ \mu V/K$ for $\delta = 0.00$, or $\alpha = -16\ \mu V/K$ for $\delta = 0.11$) and $\beta = 2$, one may estimate the composition of $LaMnO_{3+\delta}$ at that temperature; this estimate gives δ_{ht} (e.g., $\delta_{ht} = 0.16$ for $\delta = 0.00$ as starting material or $\delta_{ht} = 0.18$ for $\delta = 0.11$ as starting material). A $\delta_{ht} > \delta$ suggests that oxidation of the samples takes place during the measurements, which were made in air. The evolution of the values of $\alpha(T)$ reached at high temperatures for different δ values of the starting materials confirms that the kinetics of this oxidation reaction is reflected in the measured values of the Seebeck coefficient: the higher the nonstoichiometry δ in the starting material, the more negative the value of α reached at high temperatures and therefore the larger the nonstoichiometry δ_{ht} in the final composition. The maximum value of $\delta_{ht} = 0.18$ demonstrates that this composition represents the maximum attainable extent of oxidation or nonstoichiometry, δ, in this perovskite at 1 atm pressure.

Further experimental evidence for oxidation in air at higher temperatures is shown in Fig. 9, where the evolution of $\alpha(T)$ with temperature in air for $\delta = 0.00$ is shown in combination with results of thermogravimetric experiments. Above about 600 K, the Seebeck coefficient drops to small positive values and a mass gain in the TGA signals the onset of oxidation. On cooling, $\alpha(T)$ does not return to its original value because the sample remains oxidized. This conclusion is also confirmed by thermogravimetry in different atmospheres: (i) the higher the oxygen partial pressure in the surrounding gas atmosphere, the higher the extent of oxidation (no oxidation in argon, $\delta = 0.04$ after heating in oxygen-contaminated nitrogen, and $\delta = 0.15$ after heating in air); (ii) after oxidation, the sample mass stays constant during cooling, i.e., the sample does not give up oxygen on lowering the temperature.

Figure 10 shows the thermopower $\alpha(T)$ between 30 and 320 K for samples with values of δ ranging from 0.05 to 0.18. Similar results had been reported for some values of δ (11, 14). The trend mentioned above is clearly visible: the smaller the δ, the higher the Seebeck coefficient at $T_{\alpha(max)}$. The temperature of this maximum coincides with T_c (except for $\delta = 0.18$, where T_c is somewhat higher than $T_{\alpha(max)}$). As the temperature decreases to T_c, the factor β of Eq. [3] changes from 2 in the paramagnetic phase at high temperatures to 1 in the ferromagnetic phase; the onset of magnetic long-range order removes the spin degeneracy of the charge carriers. This change in β would lead to an enhancement of $\alpha(T)$ of up to 60 $\mu V/K$ during cooling to T_c. For $\delta \leq 0.10$, the observed change in $\alpha(T)$ is larger than that, which indicates that, in addition to a vanishing of the spin degeneracy, holes are progressively trapped out as the temperature approaches T_c. The drop of $\alpha(T)$ with decreasing temperature below T_c is remarkable; it indicates a release of the charge carriers from the traps. In the rhombohedral samples

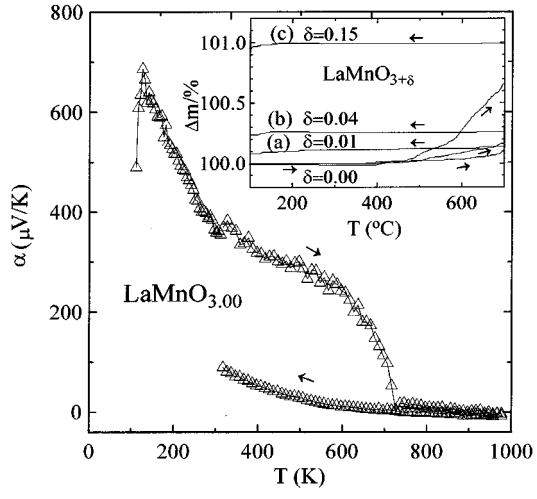

FIG. 9. Thermopower α for $\delta = 0.00$ between 100 and 1000 K during heating and cooling. (Inset) TGA curves for $\delta = 0.00$ for the temperature range 300–973 K (heating and cooling rate 1 K/min, holding at 973 K for 2 h) in different gas atmospheres: (a) Ar, $\log p_{O_2} \cong -5$; (b) N_2, $\log p_{O_2} \cong -3.5$; (c) air; values of δ represent the final compositions calculated from the mass gain.

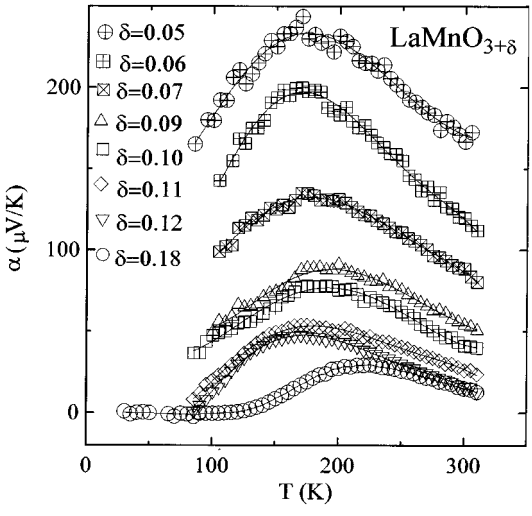

FIG. 10. Variation of thermopower with, temperature $\alpha(T)$ for selected samples between 30 and 320 K.

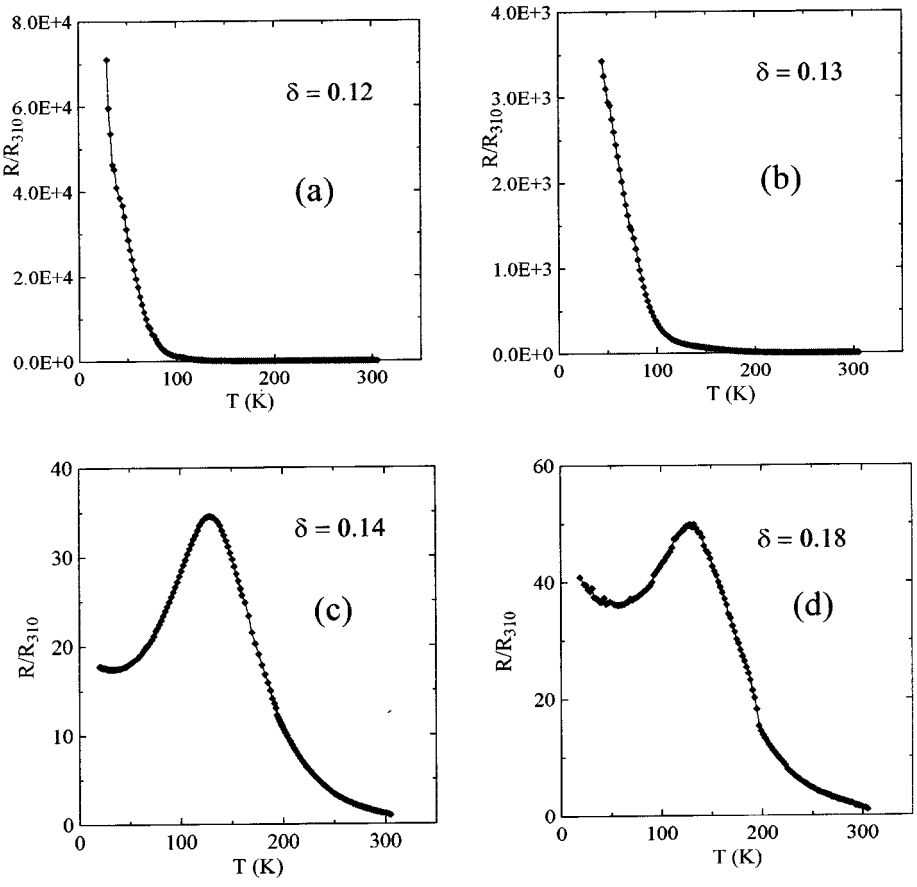

FIG. 11. Temperature dependence of the electrical resistance normalized to the resistance at room temperature between 30 and 310 K for the system $LaMnO_{3+\delta}$: (a) $\delta = 0.12$; (b) $\delta = 0.13$; (c) $\delta = 0.14$; (d) $\delta = 0.18$.

there appears to be also a change in the character of the mobile charge carriers from small polarons.

The temperature dependence of the resistance $R(T)$ for several samples is shown in Fig. 11. $LaMnO_{3+\delta}$ with $\delta \leq 0.13$ is semiconducting while for $\delta = 0.14$ and $\delta = 0.18$ a resistance maximum at 130 K is found. Below 130 K, metallic-like behavior with positive $\Delta R/\Delta T$ is observed down to 50 K; below 50 K the resistance increases again with decreasing temperature. The low density of the rhombohedral samples introduces an important grain-boundary resistance, and the resistance maximum occurs at about 80–90 K below $T_{\alpha(\max)} \approx T_c$, whereas it appears to be closer to T_c in dense samples prepared electrochemically (11).

A tentative phase diagram is proposed in Fig. 12; it includes the orthorhombic–rhombohedral transition temperature T_t as determined by Wold and Arnott (1). At values of $\delta \leq 0.10$, T_t marks the onset of the cooperative Jahn–Teller deformation that is superimposed on an orthorhombic distortion, e.g., at about 600°C for $\delta = 0.00$ (T_t for small δ not included in Fig. 12); the linear fall off of T_t with increasing δ at higher oxidation represents the orthorhombic–rhombohedral transition in the absence of a cooperative Jahn–Teller deformation. At room temperature, our data suggest a two-phase region (Fig. 2) in the interval $0.06 \leq \delta \leq 0.09$. The onset of long-range magnetic order is denoted as T_c; it is somewhat higher in the rhombohedral phase than in the O-orthorhombic phase. Below T_c, the transition with increasing δ from a canted-spin antiferromagnet at $\delta = 0.00$ to a nearly full ferromagnetic magnetization at $\delta = 0.13$ appears to be via a heterogeneous spin configuration as in a spin glass (SG), see Fig. 4. At higher δ values a metamagnetic canted-spin configuration (MCS) appears. All samples are insulators (I) in the paramagnetic phase (P) at $T > T_c$; below T_c there is a change at $\delta \approx 0.14$ from an insulating state to a peculiar electronic state (17).

DISCUSSION

1. *Electronic States*

Figure 13a presents a schematic electron-energy diagram for the MnO_3 array of the parent compound $LaMnO_{3.00}$.

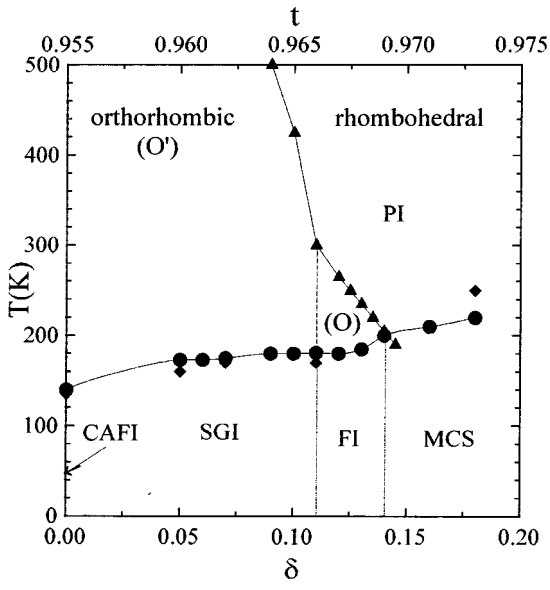

FIG. 12. Magnetic phase diagram of the system $LaMnO_{3+\delta}$. Temperature of thermopower maximum, $T_{\alpha(\max)}$ (full circles); Curie temperature, T_c, or, Neel temperature for small δ, T_N (full rhombi); temperature of the orthorhombic to rhombohedral phase transition from Ref. (1), T_t (full triangles). The full lines connecting the points are a guide for the eye. PI, paramagnetic insulator; CAFI, canted-spin antiferromagnetic insulator; SGI, magnetically heterogeneous, spin-glass-like insulator; FI, ferromagnetic insulator with, nearly complete parallel alignment of spins; MCS, metamagnetic, canted-spin configuration.

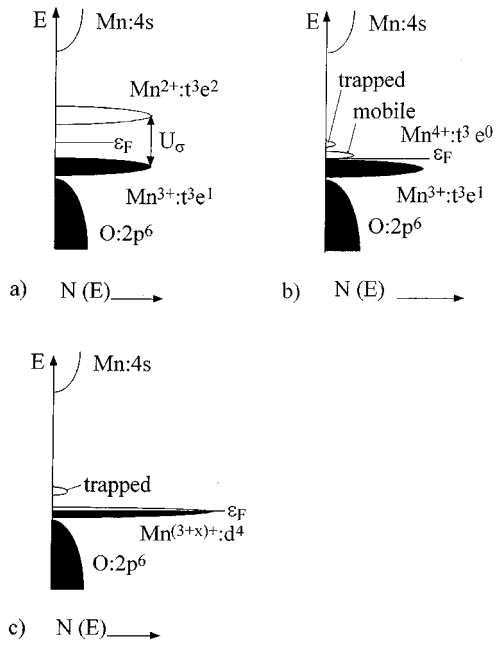

FIG. 13. Schematic band diagrams for (a) $LaMnO_{3.00}$, (b) semiconducting mixed-valence manganites with intermediate values of δ, and (c) $LaMnO_{3+\delta}$ with $\delta > 0.13$ with metallic-like resistivity below T_c.

The empty 5*d* and 6*s* bands of the La^{3+} ions overlap the Mn 4*s* band. The fact that $LaMnO_3$ and $CaMnO_3$ are both antiferromagnetic insulators places both the Mn^{3+}/Mn^{2+} and Mn^{4+}/Mn^{3+} redox couples within the relatively large energy gap between the filled $O:2p^6$ band and the empty Mn:4*s* and La:5*d*, 6*s* bands. The existence of a cooperative Jahn–Teller deformation in $LaMnO_3$ indicates that in the stoichiometric compound the octahedral site, high-spin $Mn^{3+}:d^4$ configuration is localized and separated discretely from an empty $Mn^{2+}:d^5$ configuration by the Coulomb energy U_σ required to induce the disproportionation reaction $2Mn^{3+} \rightarrow Mn^{4+} + Mn^{2+}$. In octahedral coordination, the symmetry of the cubic crystalline field splits the *d*-fold manifold into a more stable, orbitally threefold-degenerate set of *t* orbitals and a less stable, orbitally twofold-degenerate set of *e* orbitals to give the high-spin localized configurations $Mn^{2+}:t^3e^2$, $^6A_{1g}$; $Mn^{3+}:t^3e^1$, ^5E_g; and $Mn^{4+}:t^3e^0$, $^4A_{2g}$.

The Mn^{3+}/Mn^{2+} redox couple lies high enough in energy above the filled $O:2p$ orbitals that hybridization of the filled oxygen wave functions and the empty *d* wave functions at a Mn^{3+} ion may be described by second-order perturbation theory to give ligand-field orbitals (18)

$$\Psi_t = N_\pi(f_t - \lambda_\pi\phi_\pi) \quad \text{and} \quad \Psi_e = N_\sigma(f_e - \lambda_s\phi_s - \lambda_\sigma\phi_\sigma), \qquad [4]$$

where f_t and f_e are, respectively, the π- and σ-bonding atomic orbitals, the ϕ_i are symmetrized $O:2p_\sigma$, 2*s*, and $2p_\sigma$ orbitals, and the covalent mixing parameters λ_i ($\lambda_i = b_i^{ca}/\Delta E_i$) increase with the cation–anion resonance integral b_i^{ca} (i.e., with the degree of overlap of the cation and anion wave functions) and with decreasing energy ΔE_i to lift the respective oxygen electron to the corresponding empty Mn 3*d* wave function (18). In the discussion to follow, Eq. [4] is assumed to remain valid for the Mn^{4+} ions also even though the energy ΔE_σ to lift an O $2p_\sigma$ electron into an empty *e* orbital of the Mn^{4+}/Mn^{3+} couple is relatively small. The covalent mixing parameters stand in the relation

$$\lambda_s \ll \lambda_\pi < \lambda_\sigma \qquad [5]$$

and the electron–electron electrostatic energies U_π and U_σ to add an electron to a *t* or *e* manifold are in the relation

$$U_\pi > U_\sigma. \qquad [6]$$

A measure of the strength of a $(180^\circ - \phi)$ Mn–O–Mn interaction is the corresponding spin-independent cation–cation resonance integral $b_{nn} = (\Psi_i, H'\Psi_j)$ between the nearest-neighbor Mn atoms:

$$b_\pi \approx \varepsilon_\pi\lambda_\pi^2 \quad \text{and} \quad b_\sigma \approx \varepsilon_\sigma\lambda_\sigma^2\cos\phi \qquad [7]$$

In Eq. [7], the relatively small term $\varepsilon_s\lambda_s^2 \ll \varepsilon_\sigma\lambda_\sigma^2\cos\phi$ is omitted from b_σ to simplify the discussion. The tight-binding bandwidth $W_\pi \approx 2zb_{nn}$ for the antibonding π^* d-like bands with $z = 6$ nearest neighbor Mn–O–Mn interactions b_{nn} is

$$W_\pi \approx 12\varepsilon_\pi\lambda_\pi^2 < U_\pi \qquad [8]$$

so that the t^3 configurations with spin $S = 3/2$ remain localized as the $(MnO_3)^{3-}$ array is oxidized to $(MnO_3)^{2-}$ in $CaMnO_3$. Therefore it is necessary to replace b_σ and b_π by the spin-dependent resonance integrals $t_\pi = b_\pi\sin(\theta_{ij}/2)$ and $t_\sigma = b_\sigma\cos(\theta_{ij}/2)$, where θ_{ij} is the angle between spins on neighboring Mn atoms at sites R_i and R_j. Since the spin angular momentum is conserved in an electron transfer, the Pauli exclusion principle constrains the half-filled t^3 configurations at neighboring atoms to couple antiferromagnetically, which introduces a $\sin(\theta_{ij}/2)$ into t_π; however, transfer of an e electron to an empty e orbital is energetically favored, so ferromagnetic intraatomic exchange introduces a $\cos(\theta_{ij}/2)$ into t_σ. Since the t^3 configurations remain unchanged on oxidation, the antiferromagnetic $Mn:t^3$–O:$2p_\pi$–$Mn:t^3$ spin–spin interactions are described by superexchange second-order perturbation theory. The ferromagnetic $Mn:t^3e^1$–$O:2p_\sigma$–$Mn:t^3e^0$ e-electron interactions are described by superexchange third-order perturbation theory where the charge transfer is virtual because it costs an energy, e.g., U_σ in stoichiometric $LaMnO_3$, and by first-order double-exchange theory where a real $Mn^{3+} + Mn^{4+} \rightarrow Mn^{4+} + Mn^{3+}$ charge transfer is on a time scale that is fast relative to the relaxation of the $S = 3/2$ spins of the t^3 configurations. Replacemment of b_σ by t_σ gives a tight-binding bandwidth for the e electrons as

$$W_\sigma \approx 12\varepsilon_\sigma\lambda_\sigma^2\cos\phi\cos(\theta_{ij}/2). \qquad [9]$$

From the uncertainty principle, the time for a real electron transfer in a mixed-valent system is

$$\tau_h \approx h/2\pi W_\sigma \approx h/24\pi t_\sigma \qquad [10]$$

and a transition from polaronic to itinerant electronic behavior occurs as τ_h decreases to below the period $1/\omega_R$ of the optical-mode lattice vibration that would trap a hole at a distiguishable Mn^{4+} ion. Increasing t_σ by increasing λ_σ (with hydrostatic pressure to increase b_σ^{ca}) or decreasing ϕ (by increasing the tolerance factor t of Eq. [2] by choosing a larger Ln^{3+} and/or A^{2+} ion) or decreasing θ_{ij} (by introducing long-range ferromagnetic order) shortens τ_h and, at crossover from small-polaron to itinerant-electron behavior, can induce a release of holes trapped in localized states (19). It is this modulation that is responsible for the colossal magnetoresistance (CMR) found in the $Ln_{1-x}A_xMnO_3$ systems.

2. *Stoichiometric $LaMnO_3$*

In $LaMnO_{3.00}$, a cooperative Jahn–Teller distortion to remove the orbital degeneracy leads to an anisotropic magnetic order with ferromagnetic $Mn:t^3e^1$–$O:2p_\sigma$–$Mn:t^3e^0$ interactions within the a–b plane of the orthorhombic cell (*Pbnm*) and antiferromagnetic $Mn:t^3$–$O:2p_\sigma$–$Mn:t^3$ coupling between the planes in the c direction (9) (Type A magnetic order), as confirmed by neutron diffraction (10). As shown in Fig. 3, the sample with $\delta = 0.00$ exhibits a weak spin-canting ferromagnetism with an antiferromagnetic Neel temperature $T_N \approx 135$ K. The appearance of a small canting of the antiferromagnetically ordered spins arises from Dzialoshinsky's antisymmetric exchange (20). The fact that stoichiometric $LaMnO_3$ exhibits weak ferromagnetism was first noted by Matsumoto (21). The magnitude of that ferromagnetic moment is about 0.4 μ_B in $LaMnO_{3.00}$ as reported recently (22). It has been shown that, in the lightly doped material $La_{0.96}Sr_{0.04}MnO_3$ (Type-A magnetic order), the ferromagnetic component and the antiferromagnetic long-range order set in at the same temperature of 136 K (23). Above room temperature, $LaMnO_{3.00}$ shows Curie–Weiss behavior; however, the plot $1/\chi$ vs T is not a straight line (Fig. 3) and the effective magnetic moment is 5.5 μ_B per Mn ion, i.e., significantly larger than expected for a spin-only contribution of Mn^{3+}. Either local, short-range ferromagnetic interactions stabilize short-range ferromagnetic order (or superparamagnetic clusters) in this material up to temperatures of several hundred degrees above T_N or the Weiss molecular field increases with temperature. It has been reported that in the temperature range 400–470°C, a transition in the Curie–Weiss plot occurs (24–26) with an effective magnetic moment above that transition of 4.9 μ_B per Mn ion as expected for Mn^{3+} (26). Unfortunately, this temperature is above the accessible temperature range of the SQUID device used in this study. Structural transitions have been reported for nominally stoichiometric $LaMnO_{3.00}$: from orthorhombic to rhombohedral at 600°C (1) and from orthorhombic to cubic at 300°C followed by cubic to rhombohedral at 530°C (15). However, no provision was made to preserve the oxygen stoichiometry in these studies, and oxidation sets in above about 500°C in air (Figs. 8 and 9). Therefore the origin of the change in slope of the inverse-susceptibility vs temperature plot remains unresolved.

Nominally stoichiometric $LaMnO_{3.00}$ is an insulator. However, a positive thermopower indicates some oxidation ($\delta < 0.01$) in our samples, and the increase to a large positive value at a $T_{\alpha(max)} \approx T_N$ indicates a trapping out at T_N of most of the holes that are present and a release of some holes below T_N.

3. *Paramagnetic $LaMnO_{3+\delta}$*

Oxidation of the MnO_3 array lowers the Fermi energy ε_F of Fig. 13a into the Mn^{4+}/Mn^{3+} redox couple as illustrated in Fig. 13b; it also creates cation vacancies: $LaMnO_{3+\delta} = La_{1-\varepsilon}Mn_{1-\varepsilon}O_{3.00}$. Oxidation of a $Mn^{3+}:t^3e^1$ configuration to a $Mn^{4+}:t^3e^0$ configuration leaves empty e states at the top of the $Mn^{3+}:t^3e^1$ manifold of energies. Contraction of the equilibrium Mn–O bond length at a smaller Mn^{4+} ion would lift the empty e states of the Mn^{4+} ion above the top of the $Mn^{3+}:t^3e^1$ manifold. Therefore, if the time $\tau_h \approx h/2\pi W_\sigma$ for a $Mn^{3+} + Mn^{4+} = Mn^{4+} + Mn^{3+}$ charge transfer is long compared to the time to trap the hole by a breathing-mode contraction of the equilibrium Mn–O bond lengths, the holes become polaronic with energies discretely above the $Mn^{3+}:t^3e^1$ energies as shown in Fig. 13b. Cation vacancies tend to trap holes, and polaronic holes become trapped at a higher energy than mobile polarons. The distribution of holes between trapped and free polaronic states is temperature-dependent.

In the paramagnetic temperature domain, the holes remain polaronic for all compositions δ, but the concentration of mobile holes decreases with decreasing temperature. As a result, $\alpha(T)$ is described by Eq. [3], and it increases with decreasing temperature not only because the spin-degeneracy parameter changes from $\beta = 2$ to $\beta = 1$, which can give an increase of 59 μV/K, but also because trapping out of the polaronic holes decreases the effective occupancy factor c. The motional enthalpy of the diffusive motion of the mobile holes as well as the activation energy for release of the trapped holes introduce an activation energy into the conductivity, so the conductivity has a semiconductive temperature dependence. Therefore the paramagnetic domain is everywhere designated PI in Fig. 12.

The cooperative Jahn–Teller distortion that is superimposed on the O-orthorhombic deformation due to a tolerance factor $t < 1$, Eq. [2], gives an O′-orthorhombic phase, i.e., $c/a < \sqrt{2}$. Within the paramagnetic domain, the O′-orthorhombic to rhombohedral transition temperature T_t was found by Wold and Arnott (1) to decrease sharply with increased δ for $0 \leq \delta \leq 0.10$; the cooperative Jahn–Teller deformation disappears for $\delta > 0.10$, and T_t for the O-orthorhombic to rhombohedral transition decreases linearly with δ. Recently, a $T_t \cong 200$ K has been found for $\delta = 0.15$ (22). The long-range magnetic-ordering temperature T_c increases somewhat on crossing from the O-orthorhombic to the rhombohedral phase, which has a larger Mn–O–Mn bond angle and therefore a larger t_σ. Quenching from higher temperatures may give a single crystallographic phase; but a two-phase range $0.05 < \delta < 0.10$ was found (Fig. 2) in our samples, which might reflect a different quenching rate.

The evolution with δ of the paramagnetic Curie–Weiss plots (Fig. 3) shows a continuous increase of the Weiss constant θ_p with δ. With an increasing tolerance factor t, the angle ϕ decreases and the ferromagnetic Mn–O–Mn interactions introduced by the e electrons increase relative to the antiferromagnetic $Mn:t^3$–$O:2p_\pi$–$Mn:t^3$ interactions. $T_N > \theta_p > 0$ in $LaMnO_{3.00}$ shows the coexistence of antiferromagnetic and ferromagnetic interactions. The ferromagnetic component becomes more dominant in the intermediate compositions where $T_c < \theta_p$ is found, e.g., see the curves for $\delta = 0.07$ and 0.11 in Fig. 3. However, for $\delta \geq 0.14$, $T_c > \theta_p$ is remarkable, and a drop in the magnetization relative to ferromagnetic alignment of the Mn spins (Fig. 6) indicates the reappearance of a competitive antiferromagnetic coupling. Moreover, μ_{eff} significantly larger than the theoretical value, except for the $\delta = 0.18$ sample, indicates the possible presence of superparamagnetic clusters to about room temperature; trapping of holes at cation vacancies introduces a high Mn^{4+}/Mn ratio locally within a cluster where ferromagnetic Curie temperatures of up to 350 K may be supported. At higher temperatures, a Weiss molecular field that increases linearly with temperature can give an effective Curie constant, and hence μ_{eff}, that is larger than theoretical.

4. *Magnetically Ordered $LaMnO_{3+\delta}$*

Below T_c, three compositional domains can be distinguished in Fig. 12: $0 < \delta < 0.07$, $0.10 < \delta < 0.14$, and $0.14 \leq \delta \leq 0.18$. The first appears to contain ferromagnetic clusters embedded in an antiferromagnetic matrix giving rise to spin-glass (SG) magnetic behavior, see Fig. 4. With the collapse of the cooperative, static Jahn–Teller deformation associated with the O′-orthorhombic structure, the matrix becomes ferromagnetic, but some clusters may become antiferromagnetic at the higher values of δ. On passing from $\delta \approx 0.13$ to $\delta \approx 0.14$ there is a transition of the charge carriers below T_c from polaronic behavior to fast, real charge transfer between at least pairs of Mn atoms, and the magnetization exhibits a reduced magnetization with metamagnetic behavior characteristic of a spiral-spin configuration at low fields and a canted-spin configuration at high fields (MCS), see Fig. 4. The transition from a canted-spin antiferromagnetic insulator (CAFI) at $\delta = 0$ to a spin-glass insulator (SGI) at $\delta = 0.05$ is not defined by our data.

For $\delta \leq 0.06$, we postulate that the holes trapped at cation vacancies form hole-rich clusters within which the cooperative Jahn–Teller deformations become dynamic rather than static to give three-dimensional—as against two-dimensional—ferromagnetic coupling within a cluster. Moreover, ferromagnetic order within a cluster increases $\cos(\theta_{ij}/2)$ to near unity, so $\tau_h \leq h/2\pi W_\sigma$ may be shortened to where real charge transfer takes place, thus increasing the onset temperature for the formation of superparamagnetic clusters to near room temperature. Below T_c,

the O′-orthorhombic matrix orders antiferromagnetically, but with weakly canted spins as in the parent $LaMnO_{3.00}$ compound. Magnetic coupling through the antiferromagnetic matrix between superparamagnetic clusters randomly distributed in space gives rise to the spin-glass behavior. The peak in the ZFC curve of Fig. 4 for $\delta = 0.05$ is associated with the temperature of freezing of the superparamagnetic spins into different directions as a result of the competing ferromagnetic and antiferromagnetic intercluster interactions. Magnetic order within the matrix lowers the activation energy for escape of holes from the clusters to the matrix, thus introducing a sharp drop in $\alpha(T)$ on lowering the temperature through T_c.

Segregation of the SGI phase at $\delta \approx 0.06$ from the FI phase at $\delta \approx 0.10$ is consistent with a continuous increase in the magnetization through the two-phase region (Fig. 6). Comparable values of the magnetic moment (e.g., 2.5 μ_B for $\delta = 0.08$) have been reported (22).

In the range $0.10 \leq \delta \leq 0.18$, the matrix no longer sustains a cooperative, static Jahn–Teller deformation, and ferromagnetic Mn^{3+}–O–Mn^{3+} superexchange interactions are stabilized in three dimensions by strong *e*-electron coupling to the oxygen vibrations along a Mn–O–Mn bond axis between neighboring Mn atoms as has been demonstrated in the $LaMn_{1-x}Ga_xO_3$ system (27). In addition the Mn^{3+}–O–Mn^{4+} interactions are ferromagnetic either by superexchange or double exchange; evidence for fast electron transfer in compositions with $\delta \geq 0.13$ suggest a double-exchange mechanism below T_c in this compositional range. A ferromagnetic matrix couples any ferromagnetic clusters ferromagnetically. However, at these higher values of δ, the cation-vacancy concentration apparently becomes high enough that some clusters within vacancy-rich regions may contain enough Mn^{4+} ions to form antiferromagnetic domains within the ferromagnetic matrix, so the full ferromagnetic magnetization is not quite realized for $0.10 < \delta \leq 0.13$.

In the range $0.13 < \delta \leq 0.18$, the volume of the antiferromagnetic Mn^{4+}-rich clusters increases with δ. More important, the increasing value of the tolerance factor decreases the angle ϕ of bending of the Mn–O–Mn bonds from 180°, which increases W_σ in accordance with Eq. [9]. Below T_c, $\cos(\theta_{ij}/2)$ increases in the ferromagnetic matrix, and the $\alpha(T)$ curves of Fig. 10 and the R/R_{310} curves of Fig. 11 indicate that the conduction electrons are no longer small polarons; fast, real charge transfer between at least pairs of Mn^{3+} and Mn^{4+} ions occurs to give ferromagnetic double-exchange interactions. The ferromagnetic double-exchange interactions vary as $\cos(\theta_{ij}/2)$ whereas the antiferromagnetic superexchange interactions vary as $\cos\theta_{ij}$. In this situation, optimization of the angle θ_{ij} between neighboring spins can stabilize a cant angle ($0 < \theta_{ij} < 180°$) in the matrix that increases as the relative strength of the ferromagnetic double exchange decreases with increasing δ, i.e., with decreasing concentration of mobile *e* electrons. Canted spins in high fields give a net ferromagnetic moment; at low fields, this type of canting may transform into a helical spiral. We believe the metamagnetic type of increase in the magnetization with applied field in the range $0.13 < \delta \leq 0.18$ is due to transformations of ferromagnetic spiral spins in the matrix to a canted-spin ferromagnetism.

Two additional observations should be noted. Although the low density of the samples in the range $0.13 \leq \delta \leq 0.18$ renders unreliable interpretation of the R/R_{310} curves in Fig. 11, the Seebeck data of Fig. 10 should be reliable. The maximum in $\alpha(T)$ at a $T_{max} \approx T_c$ with a drop to a constant, essentially zero value below 100 K is similar to the behavior found in the system $(La_{1-x}Nd_x)_{0.7}Ca_{0.3}MnO_3$ at the critical tolerance factor t_c for a transition below T_c from small-polaron to double-exchange behavior (17). In that case, the conduction electrons do not become metallic in a conventional sense; the mobile holes become condensed into *vibronic* states (V) that show no energy dispersion as illustrated in Fig. 13c. The mobile electrons are extended over at least Mn^{3+}–O–Mn^{4+} pairs, and these pairs apparently move without any activation energy through the MnO_3 array. Our data indicate that a similar phenomenon takes place in the canted-spin matrix in the range $0.13 < \delta \leq 0.18$.

Finally, the peculiar temperature dependence of the magnetization of the $\delta = 0.16$ sample (Fig. 7) may reflect the magnetic inhomogeneity. An escape of trapped holes to the matrix with increasing temperature, which is suggested by the R/R_{310} curves of Fig. 11, would increase the ferromagnetic component of the coupling in the matrix, thereby reducing the equilibrium cant angle θ_{ij} and increasing somewhat the magnetization with increasing temperature.

CONCLUSIONS

The system $LaMnO_{3+\delta}$ contains cation vacancies, not oxygen interstitials; it corresponds to $La_{1-\varepsilon}Mn_{1-\varepsilon}O_3$. Annealing in air above 1000°C yields an O′-orthorhombic room temperature phase stable for $\delta \leq 0.06$. For $\delta \geq 0.10$, the high-temperature rhombohedral phase undergoes a transition to an O-orthorhombic structure below room temperature as a result of a decrease with temperature of the tolerance factor $t < 1$. The O′-orthorhombic structure reflects a cooperative Jahn–Teller deformation superposed on the O-orthorhombic structure. The room temperature tolerance factor t, calculated from tables of ionic radii, increases with δ through the critical value where, with increasing δ, a transition from localized to itinerant electronic behavior occurs below a ferromagnetic Curie temperature T_c. In the cation-stoichiometric perovskites $Ln_{0.7}Ca_{0.3}MnO_3$, where *Ln* may be a combination of rare-earth atoms, the critical tolerance factor is $t_c \approx 0.96$. The introduction of cation vacancies into the $LaMnO_{3+\delta}$ system perturbs the periodic potential of the $Mn_{1-\varepsilon}O_3$ array so as to shift the critical tolerance factor from 0.96 to $t_c \approx 0.97$.

The magnetic and transport data for the system $LaMnO_{3+\delta}$ reveal the presence of heterogeneous magnetic behavior for $\delta > 0$. The parent compound $LaMnO_{3.00}$ is a Type-A antiferromagnet, the cooperative Jahn–Teller deformation of the O′-orthorhombic structure stabilizing anisotropic Mn–O–Mn superexchange interactions: ferromagnetic (001) planes coupled antiparallel to one another, but with a weak ferromagnetic moment superimposed due to spin canting by an antisymmetric superexchange component. In the range $0 < \delta \leq 0.06$, where X-ray diffraction indicates a single O′-orthorhombic phase at room temperature, the magnetic data reveal stabilization of superparamagnetic clusters, presumably associated with holes trapped at cation vacancies, below room temperature; the static cooperative Jahn–Teller deformation would be suppressed within the hole-rich clusters, where strong electron coupling to dynamic Jahn–Teller deformations would give ferromagnetic superexchange interactions. The clusters are embedded in an O′-orthorhombic matrix that orders with the Type-A antiferromagnetic order below a Néel temperature T_N. Magnetic coupling between the spatially disordered ferromagnetic clusters through the antiferromagnetic matrix is frustrated and leads to spin-glass behavior.

In the O-orthorhombic and rhombohedral phases, there is no cooperative Jahn–Teller deformation, and ferromagnetic Mn^{3+}–O–Mn^{3+} superexchange interactions become isotropic, i.e., three-dimensional. The Mn^{3+}–O–Mn^{4+} interactions are also ferromagnetic, either via superexchange where charge transfer is slow or by double-exchange where it is fast relative to the period of an oxygen-atom vibration along a Mn–O–Mn bond axis. Consequently the matrix becomes ferromagnetic. However, in vacancy-rich domains there are clusters with high concentrations of Mn^{4+} ions, and charge ordering within a cluster ($Mn^{4+}:t^3e^0$–O:$2p_\pi$–$Mn^{4+}:t^3e^0$ interactions) could introduce antiferromagnetic clusters embedded in a ferromagnetic matrix in the domain $\delta > 0.11$. For $\delta \geq 0.14$, the transport data indicate the onset of double-exchange coupling below T_c, which may introduce a spin canting of the ferromagnetic matrix that increases with δ; at larger cant angles spiral-spin configurations are stabilized. The result is a relatively sharp drop in the magnetization with increasing δ and a metamagnetic type of behavior.

The transport properties show polaronic behavior in the paramagnetic phases with increased trapping out of mobile polarons with decreased temperature. However, a maximum thermopower near T_c signals that below T_c an increasing bandwidth W_σ associated with magnetic order causes a continuous release of holes from the traps on lowering the temperature through T_c. At lowest temperatures, some of the holes released from the traps tend to become retrapped; but at higher $\delta > \delta_c$, most of them appear to become condensed into a vibronic state in which mobile holes are coupled strongly to the oxygen vibrations along a Mn–O–Mn bond axis and move diffusively through the crystal without any activation energy. This peculiar electronic state gives a zero thermopower, which signals that the electron energies have no dispersion even though the conducting *e* electrons are delocalized over at least two Mn atoms.

ACKNOWLEDGMENTS

J. S. Zhou is thanked for making the transport measurements available. One of the authors (JT) thanks the DAAD for a scholarship. The NSF is also thanked for financial support.

REFERENCES

1. A. Wold and R. J. Arnott, *J. Phys. Chem. Solids* **9,** 176 (1959).
2. J. H. Kuo, H. U. Anderson, and D. M. Sparlin, *J. Solid State Chem.* **83,** 52 (1989).
3. J. A. M. van Roosmalen and E. H. P. Cordfunke, *J. Solid State Chem.* **110,** 100 (1994).
4. J. Töpfer and R. Dieckmann, in preparation.
5. B. C. Toffield and W. R. Scott, *J. Solid State Chem.* **10,** 183 (1974).
6. M. Hervieu, R. Mahesh, N. Rangavittal, and C. N. R. Rao, *Eur. J. Solid State Inorg. Chem.* **32,** 79 (1995).
7. A. Urushibara, Y. Moritomo, T. Arima, A. Asamitsu, G. Kido, and Y. Tokura, *Phys. Rev. B* **51,** 14103 (1995).
8. Y. Tomioka, A. Asamitsu, Y. Moritomo, H. Kuwahara, and Y. Tokura, *Phys. Rev. Lett.* **74,** 5108 (1995).
9. J. B. Goodenough, *Phys. Rev.* **100,** 564 (1955).
10. E. O. Wollan and W. C. Koehler, *Phys. Rev.* **100,** 545 (1955).
11. R. Mahendiran, S. K. Tiwary, A. K. Raychaudhuri, T. V. Ramakrishnan, R. Mahesh, N. Rangavittal, and C. N. R. Rao, *Phys. Rev. B* **53,** 3348 (1996).
12. J. B. Goodenough and J. M. Longo, "Landolt-Börnstein Tabellen," Vol. III/4a, Springer–Verlag, Berlin, 1970.
13. M. Verelst, N. Rangavittal, C. N. R. Rao, and A. Rousset, *J. Solid Sate Chem.* **104,** 74 (1993).
14. J. Töpfer, J. C. Grenier, and J. P. Doumerc, *J. Mater. Chem.* **6,** 1511 (1996).
15. P. Norby, I. G. Krogh Andersen, E. Krogh Andersen, and N. H. Andersen, *J. Solid State Chem.* **119,** 191 (1995).
16. J. F. Mitchell, D. N. Argyriou, C. D. Potter, D. G. Hinks, J. D. Jorgensen, and S. D. Bader, *Phys. Rev. B* **54,** 6172 (1996).
17. J. S. Zhou, W. Archibald, and J. B. Goodenough, *Nature* **381,** 770, (1996).
18. J. B. Goodenough, *Prog. Solid State Chem.* **5**, 149 (1971).
19. J. B. Goodenough, "Proceedings of the MRS Fall Meeting, Boston, 1996."
20. I. Dzialoshinsky, *J. Phys. Chem. Solids* **4,** 241 (1958).
21. G. Matsumoto, *J. Phys. Soc. Jpn.* **29,** 606 (1970).
22. B. Hauback, H. Fjellvag, and N. Sakai, *J. Solid State Chem.* **124,** 43 (1996).
23. H. Kawano, R. Kajimoto, M. Kubota, and H. Yoshizawa, *Phys. Rev. B* **53,** 2202 (1996).
24. G. H. Jonker, *Physica* **22,** 707 (1956).
25. H. Watanabe, *J. Phys. Soc. Jpn.* **16,** 433 (1961).
26. K. Kamata, T. Nakajima, T. Hayashi, and T. Nakamura, *Mater. Res. Bull.* **13,** 49 (1978).
27. J. B. Goodenough, A. Wold, R. J. Arnott, and N. Menyuk, *Phys. Rev.* **124,** 373 (1961).